



A model-based understanding of solid-oxide electrolysis cells (SOECs) for syngas production by H₂O/CO₂ co-electrolysis



Vikram Menon ^a, Qingxi Fu ^b, Vinod M. Janardhanan ^c, Olaf Deutschmann ^{a,*}

^a Institute for Chemical Technology and Polymer Chemistry, Karlsruhe Institute of Technology (KIT), 76131 Karlsruhe, Germany

^b European Institute for Energy Research (EIFER), Emmy-Noether-Str. 11, 76131 Karlsruhe, Germany

^c Department of Chemical Engineering, Indian Institute of Technology Hyderabad, Yeddumailaram, Telangana 502 205, India

HIGHLIGHTS

- 1-D and 1-D + 1-D SOEC model for syngas production.
- Model is validated with two sets of experimental data for H₂O–H₂–CO–CO₂ inlet mixtures.
- Parametric analysis using a detailed surface reaction mechanism.
- CH₄ production kinetics is numerically investigated.

ARTICLE INFO

Article history:

Received 24 March 2014

Received in revised form

24 June 2014

Accepted 1 September 2014

Available online 18 October 2014

Keywords:

Solid oxide electrolysis cell (SOEC)

Co-electrolysis

Syngas production

Numerical modeling

Reaction kinetics

ABSTRACT

High temperature co-electrolysis of H₂O and CO₂ offers a promising route for syngas (H₂, CO) production via efficient use of heat and electricity. The performance of a SOEC during co-electrolysis is investigated by focusing on the interactions between transport processes and electrochemical parameters. Electrochemistry at the three-phase boundary is modeled by a modified Butler–Volmer approach that considers H₂O electrolysis and CO₂ electrolysis, individually, as electrochemically active charge transfer pathways. The model is independent of the geometrical structure. A 42-step elementary heterogeneous reaction mechanism for the thermo-catalytic chemistry in the fuel electrode, the dusty gas model (DGM) to account for multi-component diffusion through porous media, and a plug flow model for flow through the channels are used in the model. Two sets of experimental data are reproduced by the simulations, in order to deduce parameters of the electrochemical model. The influence of micro-structural properties, inlet cathode gas velocity, and temperature are discussed. Reaction flow analysis is performed, at OCV, to study methane production characteristics and kinetics during co-electrolysis. Simulations are carried out for configurations ranging from simple one-dimensional electrochemical button cells to quasi-two-dimensional co-flow planar cells, to demonstrate the effectiveness of the computational tool for performance and design optimization.

© 2014 Elsevier B.V. All rights reserved.

1. Introduction

Solid-Oxide Electrolysis Cells (SOECs) are valued for their capacity to facilitate the production of hydrogen and syngas (H₂, CO) as well as oxygen. In comparison to the multiple dissociative methods for hydrogen or syngas production, high temperature co-electrolysis of H₂O and CO₂ combines advantages such as fast reaction rates, lowered propensity towards carbon formation and reduced cell resistance via remarkably efficient use of heat and

electricity [1]. The produced syngas can be further processed to generate liquid hydrocarbons (e.g. synthetic diesel) via Fischer–Tropsch synthesis, or be converted to methanol, dimethyl ether (DME) or methane via catalytic reactions. Thus, it is environmentally advantageous and technologically practical to supply the energy requirements of a SOEC with a sustainable yet renewable energy source (wind, solar etc.) or nuclear energy to lower the carbon footprint and limit greenhouse gas emissions. Nevertheless, proper economic assessment is necessary to underline the feasibility of such a complex process at the systems level [2]. This could further help shift focus towards alternative energy carriers, away from existing finite fossil fuel resources, due to environmental concerns.

* Corresponding author. Tel.: +49 721 608 43064; fax: +49 721 608 44805.
E-mail address: deutschmann@kit.edu (O. Deutschmann).

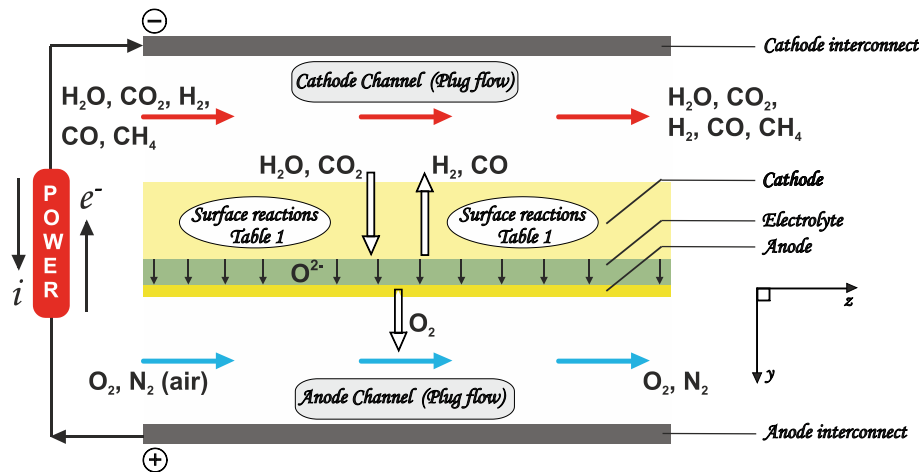


Fig. 1. Schematic representation of a planar co-flow solid oxide electrolysis cell (SOEC).

There is a wide application potential for Solid-Oxide Cells (SOCs) due to its fully reversible nature and simplicity. The representation of the planar SOEC under consideration, in this study, is shown in Fig. 1. The electrolysis reactions that contribute to the production of H₂ and CO occur at the cathode three-phase boundary (TPB) via Eqs. (1) and (2), whereas the reverse water–gas shift (RWGS) reaction occurs in the porous cathode material via Eq. (3). Although the RWGS reaction shifts towards equilibrium over nickel catalysts under reaction conditions described by Ref. [3], there is speculation as to whether it is accompanied by electrochemical/electrolysis reactions to produce CO. If so, the degree of its influence also becomes important. The oxygen production takes place at the anode TPB sites via Eq. (4). This feature was used by NASA as a proposed means for supporting life in Mars via CO₂ electrolysis on Ni- and Pt-based cathodes [4].

At the cathode-electrolyte interface,



At the porous cathode sites,



At the anode-electrolyte interface,



There is rich history pertaining to work done in the field of H₂O and CO₂ electrolysis [5–8]. The feasibility of operating high-temperature electrolysis (HTE) systems with geothermal heat has also been studied [9]. The developed techno-economic optimization model predicted the ability of a HTE system to work with geothermal temperatures as low as 230 °C. Several numerical models have also been developed to investigate performance characteristics of SOECs for hydrogen production, a summary of which is explained in Ref. [10]. Two model configurations – 1-D button cell and 1-D + 1-D planar cell were described to study the interactions between surface adsorbates, heterogeneous chemistry, and their relationship with cell performance. CO₂ electrolysis was examined at multiple temperatures in cells using a Pt–YSZ cermet electrode and a Pt electrode in order to facilitate the production of

O₂ for future human exploration in Mars [11,12]. It was found that the Pt–YSZ cermet electrode had a pronounced improvement in electrochemical characteristics, as compared to the Pt electrode, due to the distributed nature of the TPB. Additionally, CO₂ electrolysis was carried out at 850 °C in a cross-flow planar SOEC composed of a Ni–YSZ cermet electrode, YSZ electrolyte and LSM cathode [13]. A one-dimensional electrochemical model and a two-dimensional CFD model was developed and validated with the above experiment, though an analytical expression was used to describe the concentration overpotential [14]. Furthermore, a modified Butler–Volmer (B–V) equation was derived and validated for the reduction of CO₂, and employed in interfacial and distributed charge transfer models to assess electrochemical characteristics and O₂ production ability [15].

Experimental feasibility of co-electrolysis of H₂O and CO₂ for syngas production has been reported by several groups [16–19]. An electrochemical model to simulate the performance of a SOEC during co-electrolysis, considering global chemistry was illustrated [20]. A new method was proposed to quantify the contribution of RWGS to CO production or consumption, along with its dependence on operating conditions. Additionally, a 2-D CFD model to study the combined effects of heat/mass transfer and chemistry/electrochemistry in a SOEC led to the conclusion that the methanation reaction is not favored during co-electrolysis [21]. This study used a linear current-potential relationship for both H₂O and CO₂ electrolysis, which is valid only for low activation overpotentials ($\eta_{\text{act}} < 0.1$ V). A 1-D cell model coupled to elementary chemistry, validated with in-house experiments, to study the effect of cathode thickness on the interdependence of the electrochemical and chemical reaction zones was used to explain its impact on co-electrolysis operation [22]. The aforementioned authors also extended their work to study methane production characteristics, and hypothesized about pathways that led to methane formation [23]. Reduced methane formation was observed via impregnation of anti-carbon deposition catalyst Ru in the porous Ni–YSZ cathode. A similar modeling approach for syngas production using a button cell geometry coupled with heterogeneous chemistry to determine conditions for mitigating carbon deposition on the Ni surface was also reported [24]. Reversible oxygen spillover was assumed to be the charge transfer reaction, and inculcated via the commercial finite element solver – COMSOL MULTIPHYSICS.

In the present analysis, we report an in-house mathematical model that combines mass transport, heterogeneous chemistry, porous media transport and electro-chemistry. The 1-D

electrochemical model is validated with two sets of experimental data. The first set is obtained from literature [17], and the second set of experiments was performed at EIFER [25]. Unlike approximations made in literature, modified B–V equations are considered for the reduction of both CO₂ and H₂O, by considering multi-step single electron transfer reactions. Additionally, the estimated electrochemical parameters are employed in a quasi-2-D model for parametric analysis. The thermo-catalytic chemistry is handled by a 42-step elementary heterogeneous reaction mechanism for Ni catalysts, which consists of 6 gas-phase species and 12 surface adsorbed species. Reaction flow analysis is carried out in a perfectly mixed batch reactor, at OCV, to clearly understand the source of methane formation in the system. The code is available as a part of the DETCHEM™ software package [26].

2. Modeling approach

2.1. Channel flow

The quasi-two-dimensional co-flow planar model solves for the gas channels by assuming plug flow [27]. The axial diffusion is negligible compared to the axial convective transport. The radial variation in species composition is neglected as diffusive mixing is assumed to be predominant. Since the channel dimensions considered are quite small (~1 mm), the plug flow assumption is adequate to represent species transport in the channels. Thus, the model has a fixed number of cells/nodes in the axial direction, and no radial meshing. This obviously tends to have an impact on the accuracy of the computed solution. The plug flow equation for species continuity in the channels is given by

$$\frac{\partial(\rho_f Y_k)}{\partial t} = -\frac{\partial(\rho_f v Y_k)}{\partial z} + \frac{P_e}{A_c} J_k W_k, \quad k = 1, \dots, K_g \quad (5)$$

The velocity in the channel can be calculated from

$$\frac{\partial(\rho_f v)}{\partial t} = -\frac{\partial(\rho_f v v)}{\partial z} + v \sum_{k=1}^{K_g} \frac{P_e}{A_c} J_k W_k \quad (6)$$

where P_e is the perimeter associated with the electrochemically active membrane electrode assembly (MEA), ρ_f is the fluid density, Y_k is the species mass fraction of species k , v is the velocity, z is the axial position, W_k is the species molecular weight, and A_c is the cross-sectional area of the channel. Assuming constant pressure in the channels, the density is calculated from the ideal gas equation

$$p\bar{W} = \rho_f RT \quad (7)$$

with \bar{W} given as

$$\bar{W} = \sum_{k=1}^{K_g} X_k W_k \quad (8)$$

In Eqs. (5) and (6), J_k is the flux at the electrode channel interface, which is calculated using the dusty-gas model (DGM) as described below. These species molar fluxes depend on the heterogeneous chemistry within the porous-electrode structure and local current density $i(z)$. The 1-D electrochemical model, used in this study, does not solve for species transport in the gas channels.

2.2. Porous media transport

The reaction-diffusion equation for species transport in the electrodes is solved one-dimensionally along its thickness, transverse to the direction of axial flow in the channel for the quasi-2-D

co-flow planar model. The 1-D electrochemical button cell model solves the governing equations along its discretized axi-symmetric line. The transient form of the equation is given by

$$\frac{\partial(\phi \rho_f Y_k)}{\partial t} = -\frac{\partial(J_k W_k)}{\partial y} + \dot{s}_k W_k A_s, \quad k = 1, \dots, K_g \quad (9)$$

The total density of the fluid within the porous structure can be computed from

$$\frac{\partial(\phi \rho_f)}{\partial t} = -\sum_{k=1}^{K_g} \frac{\partial(J_k W_k)}{\partial y} + \sum_{k=1}^{K_g} \dot{s}_k W_k A_s \quad (10)$$

Here, \dot{s}_k is the heterogeneous molar production rate of the chemical species k , y is the independent spatial variable along the thickness, and A_s is the specific catalyst area available for surface reactions. The species molar flux J_k in the porous bed is evaluated using DGM equation as

$$J_k = -\left[\sum_{l=1}^{K_g} D_{kl}^{\text{DGM}} \nabla [X_l] + \left(\sum_{l=1}^{K_g} \frac{D_{kl}^{\text{DGM}} [X_l]}{D_{l, \text{Kn}}^e} \right) \frac{B_g \nabla p}{\mu} \right] \quad (11)$$

The DGM is written as an implicit relationship between the pressure gradient, concentration gradients, molar fluxes and molar concentrations. It neglects the effect of external forces and thermo-diffusion. The porous medium is considered to be a stationary component of the mixture in which the Chapman–Enskog kinetic theory is used to estimate the binary diffusivities, while the pressure variations are proportional to the variations in gas concentrations [28]. Since the flux ratios among gas species become complicated for multi-component H₂–H₂O–CO–CO₂ systems, the equimolar counter diffusion assumption is no longer valid. In this scenario, the DGM is recommended, over the Fick's model (FM) or the Stefan–Maxwell model (SMM), to resolve flux ratios using Graham's law of diffusion in parallel with fluxes occurring due to electrochemistry [29]. This justifies the usage of the DGM despite its computational expense. The first term on the right-hand side of Eq. (11) represents the diffusive flux and the second term represents the viscous flux. D_{kl}^{DGM} is defined as the DGM diffusion coefficients and is formulated as

$$D_{kl}^{\text{DGM}} = H^{-1} \quad (12)$$

where the elements of the H matrix are

$$h_{kl} = \left[\frac{1}{D_{k, \text{Kn}}^e} + \sum_{j \neq k} \frac{X_j}{D_{kj}^e} \right] \delta_{kl} + (\delta_{kl} - 1) \frac{X_k}{D_{kl}^e} \quad (13)$$

The permeability B_g in Eq. (11) is given by the Kozeny–Carman relationship [30]

$$B_g = \frac{\phi^3 d_p^2}{72\tau(1-\phi)^2} \quad (14)$$

Here, d_p is the particle diameter and τ is the tortuosity. The effective Knudsen diffusion coefficient $D_{k, \text{Kn}}^e$ in Eq. (13) is given by

$$D_{k, \text{Kn}}^e = \frac{\phi d_{\text{pore}}}{\tau} \sqrt{\frac{8RT}{\pi W_k}} \quad (15)$$

Solution of Eq. (9) requires the reaction source terms \dot{s}_k and boundary conditions at the electrode–gas chamber and electrode–electrolyte interfaces. At the electrode–gas chamber interface the inlet mass fractions serve as the boundary condition, while at

the electrode–electrolyte interface the chemical species fluxes are zero. The electrochemical reaction source terms enter as fluxes at the electrode–electrolyte interface.

2.3. Electrochemistry

The charge transfer chemistry occurs at the three-phases boundaries (TPB), which are basically interfaces formed by the electro-catalyst, electrolyte and gas-phase boundaries. In this study, we only consider charge transfer occurring at the electrode–electrolyte interface (interfacial charge transfer) and not across the utilization region of the electrodes (distributed charge transfer). The net current density, with respect to electrochemically active species – H₂O/H₂ and CO₂/CO, is computed as the normalized sum of currents – i_{H_2} and i_{CO} through two parallel pathways of charge transfer. Here, symbols with the subscript ‘H₂’ correspond to the pathway involving H₂O electrolysis, while those with the subscript ‘CO’ correspond to the accompanying parallel pathway involving CO₂ electrolysis. The two analogous electro-chemical reactions normalize to a single value of current density via charge and mass conservation equations. The potential balance equation in each pathway is formulated after taking into account all the irreversibilities (resistances) that occur during operation and is related to the current density by

$$E_{\text{cell}} = E_{\text{rev},H_2} + |\eta_a(i_{H_2})| + \eta_c(i_{H_2}) + \eta_{\text{ohm}}(i_{H_2}) + \eta_{\text{conc}}(i_{H_2}) \quad (16)$$

$$E_{\text{cell}} = E_{\text{rev},CO} + |\eta_a(i_{CO})| + \eta_c(i_{CO}) + \eta_{\text{ohm}}(i_{CO}) + \eta_{\text{conc}}(i_{CO}) \quad (17)$$

where η_a and η_c are the activation overpotentials at the anode and cathode respectively, η_{ohm} is the ohmic overpotential, and η_{conc} is the concentration overpotential. The concentration overpotential is not treated explicitly as porous media transport is modeled in detail, i.e., the reversible potential is calculated using gas-phase concentrations at the electrode–electrolyte interface. E_{rev} is the ‘reversible’ cell voltage, which is the maximum possible potential that can be derived from a cell operating reversibly, and is given by the Nernst equation as

$$E_{\text{rev},H_2} = E_{H_2}^0 + \frac{RT}{2F} \ln \left(\frac{p_{H_2,c} p_{O_2,a}^{1/2}}{p_{H_2O,c}} \right) \quad (18)$$

$$E_{\text{rev},CO} = E_{CO}^0 + \frac{RT}{2F} \ln \left(\frac{p_{CO,c} p_{O_2,a}^{1/2}}{p_{CO_2,c}} \right) \quad (19)$$

where E^0 is the electromotive force (EMF) at standard pressure, p_i represents the partial pressures of H₂, H₂O, CO, CO₂ (at the cathode TPB) and O₂ (at the anode TPB). The temperature dependent E^0 is calculated from thermodynamic data ($\Delta G(T)/2F$). The ohmic overpotential in Eqs. (16) and (17) is given by

$$\eta_{\text{ohm}} = R_{\text{tot}} i \quad (20)$$

where R_{tot} is given by

$$R_{\text{tot}} = R_e + R_c + R_{\text{LSM}} + R_{\text{Ni-YSZ}} \quad (21)$$

The magnitudes of these resistances depend on the type of material used and the micro-structure of the porous electrode. In modern cells, the electronic resistances of both electrodes R_{LSM} , $R_{\text{Ni-YSZ}}$ and the contact resistances between solid–solid interfaces

R_c are negligible compared to the ionic resistance of the electrolyte R_e , which is given by

$$R_e = \frac{l_e}{\sigma_e} \quad (22)$$

where l_e is the thickness of the electrolyte, and σ_e is the electrolyte conductivity, with the SI unit – S m⁻¹, which varies as a strong function of temperature as

$$\sigma_e = \sigma_0 T^{-1} \exp\left(\frac{-E_{el}}{RT}\right) \quad (23)$$

Here, E_{el} is the activation energy for ion transport (80.0 kJ mol⁻¹) and σ_0 is the pre-exponential factor (3.6×10^5 S cm⁻¹) [31]. The modified B–V equation is used to describe the functional relationship between the activation losses and current density by considering the rate-limiting step among elementary charge transfer pathways. For the electrochemical reduction of H₂O [32], this takes the form

$$i_{H_2} = i_{0,H_2} \left[\exp\left(\frac{(1 + \beta_a)F\eta_c}{RT}\right) - \exp\left(\frac{-\beta_c F\eta_c}{RT}\right) \right] \quad (24)$$

The modified B–V equation for the electrochemical reduction of CO₂ [15] is

$$i_{CO} = i_{0,CO} \left[\exp\left(\frac{\beta_a F\eta_c}{RT}\right) - \exp\left(-\frac{(1 + \beta_c)F\eta_c}{RT}\right) \right] \quad (25)$$

For the O₂ electrode, the B–V equation for oxygen production [32] can be described as

$$i_i = i_{0,O_2} \left[\exp\left(\frac{\beta_a F\eta_a}{RT}\right) - \exp\left(-\frac{\beta_c F\eta_a}{RT}\right) \right] \quad (26)$$

where i is the current, i_0 is the exchange current density, η is the activation overpotential, F is the Faraday constant, T is the temperature and β is the asymmetric charge transfer coefficient. The subscript index i refers to either H₂ or CO, as Eq. (26) involves two anode activation overpotentials for each charge transfer pathway, based on the type of electrolysis. The exchange current density is expressed as a function of temperature, and partial pressure of products and reactants (obtained due to its coupling with the micro-kinetic model) participating in the charge transfer chemistry, although it makes more physical sense to express it as a function of open surface coverage and surface current coverage of electrochemically active species. The exchange current densities i_{0,H_2} , $i_{0,CO}$ and i_{0,O_2} (for $\beta = 0.5$) are expressed as:

$$i_{0,H_2} = i_{H_2O}^* \frac{(p_{H_2}/p_{H_2}^*)^{1/4} (p_{H_2O})^{3/4}}{1 + (p_{H_2}/p_{H_2}^*)^{1/2}} \quad (27)$$

$$i_{0,CO} = i_{CO_2}^* \frac{(p_{CO_2}/p_{CO})^{1/4}}{1 + (p_{CO}/p_{CO}^*) + (p_{CO}/p_{CO_2}^*)} \quad (28)$$

$$i_{0,O_2} = i_{O_2}^* \frac{(p_{O_2}/p_{O_2}^*)^{1/4}}{1 + (p_{O_2}/p_{O_2}^*)^{1/2}} \quad (29)$$

where p is the partial pressure and p^* is the equilibrium pressure. The formulas and values for these parameters along with its derivation can be found in Refs. [15,32]. An Arrhenius expression is

Table 1
Heterogeneous surface reaction mechanism [35].

	Reaction	A^{\ddagger} (cm, mol, s)	E_a^{\ddagger} (kJ mol ⁻¹)	β^{\ddagger} [-]
R1	H ₂ + 2Ni(s) → 2H(s)	1.000·10 ^{-02b}	0.0	0.0
R2	2H(s) → 2Ni(s) + H ₂	2.545·10 ⁺¹⁹	81.21	0.0
R3	O ₂ + 2Ni(s) → 2O(s)	1.000·10 ^{-02b}	0.0	0.0
R4	2O(s) → 2 Ni(s) + O ₂	4.283·10 ⁺²³	474.95	0.0
R5	CH ₄ + Ni(s) → CH ₄ (s)	8.000·10 ^{-03b}	0.0	0.0
R6	CH ₄ (s) → CH ₄ + Ni(s)	8.705·10 ⁺¹⁵	37.55	0.0
R7	H ₂ O + Ni(s) → H ₂ O(s)	1.000·10 ^{-01b}	0.0	0.0
R8	H ₂ O(s) → H ₂ O + Ni(s)	3.732·10 ⁺¹²	60.79	0.0
R9	CO ₂ + Ni(s) → CO ₂ (s)	1.000·10 ^{-05b}	0.0	0.0
R10	CO ₂ (s) → CO ₂ + Ni(s)	6.447·10 ⁺⁰⁷	25.98	0.0
R11	CO + Ni(s) → CO(s)	5.000·10 ^{-01b}	0.0	0.0
R12	CO(s) → CO + Ni(s)	3.563·10 ⁺¹¹	111.27 – 50θ _{CO(s)}	0.0
R13	CH ₄ (s) + Ni(s) → CH ₃ (s) + H(s)	3.700·10 ⁺²¹	57.7	0.0
R14	CH ₃ (s) + H(s) → CH ₄ (s) + Ni(s)	6.034·10 ⁺²¹	61.58	0.0
R15	CH ₃ (s) + Ni(s) → CH ₂ (s) + H(s)	3.700·10 ⁺²⁴	100.0	0.0
R16	CH ₂ (s) + H(s) → CH ₃ (s) + Ni(s)	1.293·10 ⁺²³	55.33	0.0
R17	CH ₂ (s) + Ni(s) → CH(s) + H(s)	3.700·10 ⁺²⁴	97.10	0.0
R18	CH(s) + H(s) → CH ₂ (s) + Ni(s)	4.089·10 ⁺²⁴	79.18	0.0
R19	CH(s) + Ni(s) → C(s) + H(s)	3.700·10 ⁺²¹	18.8	0.0
R20	C(s) + H(s) → CH(s) + Ni(s)	4.562·10 ⁺²²	161.11	0.0
R21	CH ₄ (s) + O(s) → CH ₃ (s) + OH(s)	1.700·10 ⁺²⁴	88.3	0.0
R22	CH ₃ (s) + OH(s) → CH ₄ (s) + O(s)	9.876·10 ⁺²²	30.37	0.0
R23	CH ₃ (s) + O(s) → CH ₂ (s) + OH(s)	3.700·10 ⁺²⁴	130.1	0.0
R24	CH ₂ (s) + OH(s) → CH ₃ (s) + O(s)	4.607·10 ⁺²¹	23.62	0.0
R25	CH ₂ (s) + O(s) → CH(s) + OH(s)	3.700·10 ⁺²⁴	126.8	0.0
R26	CH(s) + OH(s) → CH ₂ (s) + O(s)	1.457·10 ⁺²³	47.07	0.0
R27	CH(s) + O(s) → C(s) + OH(s)	3.700·10 ⁺²¹	48.1	0.0
R28	C(s) + OH(s) → CH(s) + O(s)	1.625·10 ⁺²¹	128.61	0.0
R29	H(s) + O(s) → OH(s) + Ni(s)	5.000·10 ⁺²²	97.9	0.0
R30	OH(s) + Ni(s) → H(s) + O(s)	1.781·10 ⁺²¹	36.09	0.0
R31	H(s) + OH(s) → H ₂ O(s) + Ni(s)	3.000·10 ⁺²⁰	42.7	0.0
R32	H ₂ O(s) + Ni(s) → H(s) + OH(s)	2.271·10 ⁺²¹	91.76	0.0
R33	OH(s) + OH(s) → H ₂ O(s) + O(s)	3.000·10 ⁺²¹	100.0	0.0
R34	H ₂ O(s) + O(s) → OH(s) + OH(s)	6.373·10 ⁺²³	210.86	0.0
R35	C(s) + O(s) → CO(s) + Ni(s)	5.200·10 ⁺²³	148.1	0.0
R36	CO(s) + Ni(s) → C(s) + O(s)	1.354·10 ⁺²²	116.12 – 50θ _{CO(s)}	-3.0
R37	CO(s) + O(s) → CO ₂ (s) + Ni(s)	2.000·10 ⁺¹⁹	123.6 – 50θ _{CO(s)}	0.0
R38	CO ₂ (s) + Ni(s) → CO(s) + O(s)	4.653·10 ⁺²³	89.32	-1.0
R39	CO(s) + H(s) → HCO(s) + Ni(s)	4.019·10 ⁺²⁰	132.23	-1.0
R40	HCO(s) + Ni(s) → CO(s) + H(s)	3.700·10 ⁺²¹	0.0 + 50θ _{CO(s)}	0.0
R41	HCO(s) + Ni(s) → CH(s) + O(s)	3.700·10 ⁺²⁴	95.8	-3.0
R42	CH(s) + O(s) → HCO(s) + Ni(s)	4.604·10 ⁺²⁰	109.97	0.0

Total surface site density $\Gamma = 2.66 \times 10^{-09}$ mol cm⁻².

**s) ~ (Ni) represents a single site on the active catalytic surface.

^a Arrhenius parameters for the rate constant is written as: $k = AT^{\beta} \exp(-E_a/RT)$.

^b Sticking coefficient.

used to describe the temperature dependence of exchange current density in the form of i_i^* , which is given by

$$i_i^* = k_i \exp\left(-\frac{E_i}{RT}\right) \quad (30)$$

where the subscript index i refers to either H₂O, CO₂ or O₂. Due to the fact that the TPB sites are shared by both H₂O and CO₂, a factor γ is introduced to normalize the net current density and account for the relative percentages of H₂O and CO₂ at the electrode–electrolyte interface. Therefore, the net current density reduces to

$$i = I_{H_2} + I_{CO} = \gamma i_{H_2} + (1 - \gamma) i_{CO} \quad (31)$$

where,

$$\gamma = \frac{Y_{H_2O}^{TPB}}{Y_{H_2O}^{TPB} + Y_{CO_2}^{TPB}} \quad (32)$$

This normalization factor approach has been established and validated [33,34]. However, it is independent of certain factors affecting the TPB such as ratio of ionic to electronic particles, co-

ordination number of ionic and electronic particles, fraction overlap between these particles, volume fraction of these constituents, foreign impurities in the TPB and degradation effects on the Ni catalyst.

2.4. Thermo-catalytic chemistry

A modified Arrhenius expression, based on mean field approximation, is used for the calculation of the forward reaction rate constant for the i th thermo-catalytic reaction in the cathode according to.

$$k_{fi} = A_i \left(\frac{T}{T_0}\right)^{\beta_i} \exp\left(-\frac{E_{ai}}{RT}\right) \prod_{k=K_g+1}^{K_g+K_s} \theta_k^{\mu_{ki}} \exp\left(-\frac{\varepsilon_{ki}\theta_k}{RT}\right) \quad (33)$$

Here, A_i is the pre-exponential factor, E_{ai} is the activation energy, μ_{ki} and ε_{ki} are parameters modeling the order and activation energy dependency on surface coverage, respectively, for the i th reaction, β_i is the temperature exponent, θ_k is the surface coverage, R the gas constant, K_s is the number of surface species, K_g is the number of gas phase species and T is the temperature. The temporal variations of surface coverage θ_k is given by

$$\frac{d\theta_k}{dt} = \frac{\dot{s}_k \sigma_k}{\Gamma}, \quad k = K_g + 1, \dots, K_g + K_s \quad (34)$$

where σ_k is the co-ordination number (number of sites required for a species for adsorption), Γ the surface site density (a value of 2.66×10^{-9} mol cm⁻² is considered in this study) and \dot{s}_k is the surface production rate of species k , which is equal to

$$\dot{s}_k = \sum_{i=1}^{K_r} \nu_{ki} k_{fi} \prod_{k=1}^{K_g+K_s} [X_k]^{\nu'_{ki}} \quad (35)$$

Here, K_r is the number of surface reactions, $[X_k]$ is the concentration of species k , ν_{ki} the difference in stoichiometric coefficients of products and reactants, and ν'_{ki} are the stoichiometric coefficients of reactants. At steady state, in Eq. (34) – $\dot{s}_k = 0$ for surface species, implying no variation in surface coverage with time (although varying spatially).

The detailed multi-step heterogeneous reaction mechanism, given in Table 1, takes into account the adsorption/desorption of H₂, O₂, CH₄, CO, CO₂ and H₂O from the surface of Ni [35]. It also encompasses the water–gas shift reaction, formation of carbon monolayer, methanation reactions, steam reforming, dry reforming, partial and total oxidation of C₁ species. It was made thermodynamically consistent and extended to temperatures between 220 and 1700 °C. Furthermore, it was validated and tested with experimental data obtained from methane reforming over nickel/alumina monoliths in the temperature range of 900–1350 K, and with additional data from literature [27,32,36,37].

2.5. Computational scheme

The governing equations that are solved vary based on the geometric configuration. The planar configuration solves the governing equations in 1-D + 1-D, while the 1-D electrochemical button cell model solves the governing equations along its discretized axi-symmetric line. In the former model, the porous media is resolved along its thickness for every axial node in the channel. However, the 1-D model does not solve for gas flow in the channels. Both the models solve for the reaction-diffusion equation along the discretized porous media, whose molar flux is calculated using the DGM, with the provision of two boundary conditions. The first boundary condition at the electrode–gas chamber interface is given by the mass fractions in the gas channel. The second boundary condition equates to species fluxes that are calculated based on local current density at the electrode–electrolyte

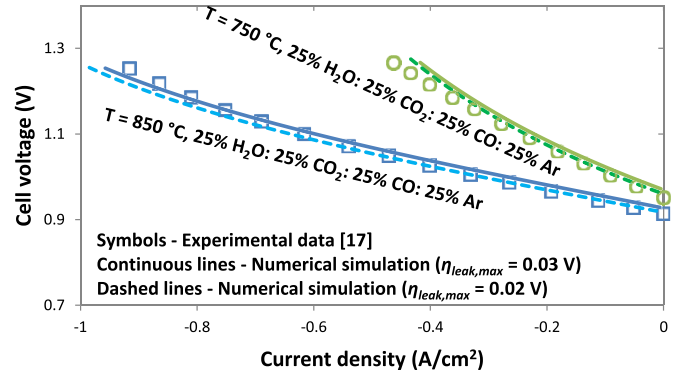


Fig. 3. Comparison between numerical simulation and experiments performed at DTU Energy conversion (former Risø DTU) [17].

interface. Time integration of Eqs. (9) and (10) is performed, until steady state, to yield species mass fractions in the porous media. Thus, at the electrode–electrolyte interface, the molar fluxes of the electrochemically active species can be specified as

$$J_{H_2O} = -J_{H_2} = \frac{I_{H_2}}{2F}; J_{CO_2} = -J_{CO} = \frac{I_{CO}}{2F}; J_{O_2} = -\frac{(I_{H_2} + I_{CO})}{4F} \quad (36)$$

Eqs. (5)–(7), (9)–(11) and (34) form a system of coupled non-linear equations, which can be treated as a differential-algebraic system mathematically. They are solved using the finite-volume method [10,32]. For the 1-D + 1-D model, a marching algorithm is used as the numerical approach. Since isothermal conditions are assumed, the reaction rates are calculated at constant inlet temperature. The equation system is solved using the differential algebraic equation (DAE) solver LIMEX [38]. A damped Newton iteration algorithm is applied to solve the system of algebraic model equations (Eqs. (16), (17), (24)–(26)) to obtain the current density in each of the parallel electrochemical pathways. The software is written in FORTRAN and is a part of the software package DETCHEM™ [26].

3. Experimental setup

Two sets of experimental data are used to numerically validate the model. The first set of experiments was performed at DTU Energy conversion (former Risø DTU). The cell was composed of a NiO/YSZ porous support layer, NiO/YSZ fuel electrode, YSZ electrolyte and LSM/YSZ oxygen electrode whose thicknesses were

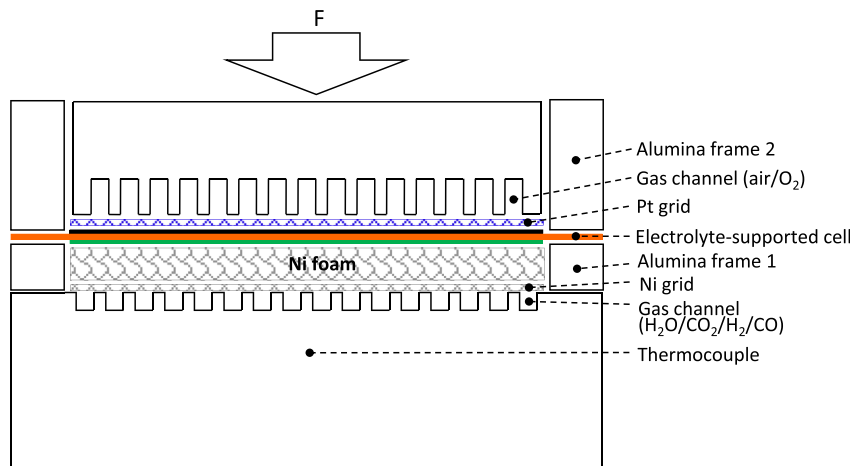


Fig. 2. Schematic illustration of the ceramic cell housing at EIFER.

Table 2
Electrochemical model/input parameters for experiments done at DTU energy conversion (former Risø DTU) [17].^a

	H ₂ –H ₂ O	CO–CO ₂
<i>Property</i>		
Fuel electrode asymmetry factor (β_a)	0.7	0.5
Oxygen electrode asymmetry factor (β_a)	0.1	0.1
<i>Exchange current density parameters</i>		
Pre-exponential factor (k_i) (A cm ⁻²)	594113.87	16129714.99
Activation energy (E_i) (J mol ⁻¹)	108.4 × 10 ³	131.38 × 10 ³
Pre-exponential for O ₂ production (k_{O_2}) (A cm ⁻²)	41783.22	
Activation energy for O ₂ production (E_{O_2}) (J mol ⁻¹)	88.75 × 10 ³	

^a Fitted with experimental data.

300 μm, 10–15 μm, 10–15 μm and 15–20 μm respectively. The inlet flow rate of pure oxygen to the LSM/YSZ electrode was 20 l h⁻¹ for all experiments. Planar Ni/YSZ supported SOC of 5 × 5 cm², with an active electrode area of 4 × 4 cm², were used in the experiments. The NiO in the Ni/YSZ electrode was reduced to nickel with hydrogen at 1000 °C, at start-up.

As described in Ref. [25], the SOC used in the second set of experiments performed at EIFER is procured from H.C. Starck (cell type ESC2). It is composed of a TZ3Y (3 mol% Y₂O₃-stabilized ZrO₂) electrolyte (50 × 50 mm² area, 90 μm thick), NiO/GDC (gadolinium-doped ceria) anode (40 × 40 mm² area, 40 μm thick) and 8YSZ/LSM–LSM (8YSZ: 8 mol% Y₂O₃-stabilized ZrO₂, LSM: lanthanum strontium manganite) double-layer cathode (40 × 40 mm² area, 40 μm thick). Although the literature reports results carried out only at 860 °C, experiments pertaining to a temperature of 810 °C

Table 3
Cell parameters and properties used for model validation/analysis.

Parameter	Model validation [17]	Model validation (EIFER)	Parametric analysis
<i>Gas channels (planar)</i>			
Length (cm)	–	–	5
Height (mm)	–	–	1
Width (mm)	–	–	1
Air inlet velocity (m s ⁻¹)	–	–	2.0
Fuel inlet velocity (m s ⁻¹)	–	–	0.3
<i>Fuel electrode</i>			
Thickness (μm)	315	40	315
Porosity (%)	35	35	35
Tortuosity	5.0	3.5	3.5
Particle diameter (μm)	1.0	2.5	2.5
Pore diameter (μm)	0.22	1.0	1.0
Specific area (m ⁻¹)	1.025 × 10 ⁵	1.025 × 10 ⁵	1.025 × 10 ⁵
<i>Electrolyte</i>			
Thickness (μm)	15	90	15
<i>Oxygen electrode</i>			
Thickness (μm)	20	40	20
Porosity (%)	35	35	35
Tortuosity	5.0	3.5	3.5
Particle diameter (μm)	1.0	2.5	2.5
Pore diameter (μm)	0.22	1.0	1.0
Specific area (m ⁻¹)	1.025 × 10 ⁵	1.025 × 10 ⁵	1.025 × 10 ⁵
<i>Operating conditions</i>			
Pressure (bar)	1.0	1.0	1.0
Temperature (°C)	750, 850	810, 860	800, 900
<i>Inlet gas composition</i>			
At the cathode	25% H ₂ O: 25% CO ₂ : 25% CO: 25% Ar	As per figure	As per figure
At the anode	Pure O ₂	21% O ₂ + 79% N ₂ (air)	21% O ₂ + 79% N ₂ (air)
<i>Leakage</i>			
$\eta_{\text{leak,max}}$ (V)	0.02, 0.03	0.05	0
i_{max} (A cm ⁻²)	1.0	1.7	0

were also performed and used in this study. The ceramic cell housing used for cell testing at EIFER is schematically shown in Fig. 2. The current collection is achieved using a Ni-grid and Ni-foam at the fuel electrode, while a Pt-grid is used at the air electrode. Gas inlets and outlets are symmetrical. As a result, the MEA may be tested in both co-flow and counter-flow configurations. It should be noted, however, that the model validation is done using experimental data that was obtained with the latter configuration. The sealing of the fuel chamber relies on the smooth surfaces of the electrolyte layer and adjacent alumina frames. The air chamber is not sealed, but is always swept with 500 sccm air. A thermocouple is inserted through a drilled hole in the anode frame, and is located at about 5 mm under the central point of the cell. The cell temperature is thus obtained, which is usually different from the oven temperature. A bubbler humidifier is used to supply steam to the cell. The polarization curves (i – V curves) were recorded by ramping the current through the cell at 5 A min⁻¹ from $i = 0$ A.

4. Results and discussion

4.1. 1-D electrochemical model

4.1.1. Model validation

The model is validated with the first set of experiments performed at DTU Energy conversion (former Risø DTU) [17]. According to the article, the authors elucidate on various loss mechanisms and reaction pathways involved in reversible SOCs via thorough DC and AC characterization (by Electrochemical Impedance Spectroscopy (EIS)) of the system. They studied electrochemical reduction and oxidation phenomena in H₂O–H₂, CO₂–CO and H₂–H₂O–CO–CO₂ mixtures to analyze the role of the WGS/RWGS reaction. Fig. 3 portrays good agreement between numerical simulation results and experimental data, measured at 750 °C and 850 °C with an inlet gas composition of 25% H₂O: 25% CO₂: 25% CO: 25% Ar to the Ni/YSZ electrode. The numerical calculations are performed using the button cell model. A leakage overpotential is considered in each of the potential balance Eqs. (16) and (17), as the experimentally measured OCV differs from the thermodynamically estimated one, and is formulated as

$$\eta_{\text{leak}} = \eta_{\text{leak,max}} \left(1 - \frac{i}{i_{\text{max}}} \right) \quad (37)$$

where i_{max} is the maximum current and a fit parameter. Here, we use $\eta_{\text{leak,max}} = 0.03, 0.02$ V and $i_{\text{max}} = 1.0$ A cm². The calculated ASR values at 1.1 V are 0.287 Ω cm² at 850 °C and 0.593 Ω cm² at 750 °C. The ASR values correspond to the case where $\eta_{\text{leak,max}} = 0.02$ V. Firstly, electrochemical input parameters are determined, through model validation, by making individual fits for varying compositions of H₂O–H₂ and CO₂–CO at 750 and 850 °C [34]. After calibration, the model is then validated for H₂O–CO₂–H₂–CO mixtures. The electrochemical parameters used for reproducing the experimental data are listed in Table 2. The values of thicknesses of the electrodes and electrolyte, along with cell properties used in model validation are listed in Table 3. It is important to note that micro-structural properties are assumed to be within a realistic range, due to its unavailability in the aforementioned literature.

Further, a second set of experiments performed at EIFER is numerically simulated to facilitate model validation. In the experiments, electrolysis was carried out with the supply of H₂O–CO₂–H₂ mixtures to the NiO–GDC cathode and air to the 8YSZ/LSM–LSM double-layer anode. The experiments were carried out at 810 and 860 °C with multiple cathode inlet gas compositions. Supplementary information about the setup can be found in Section 3. It was observed that the ASR values for electrolysis in

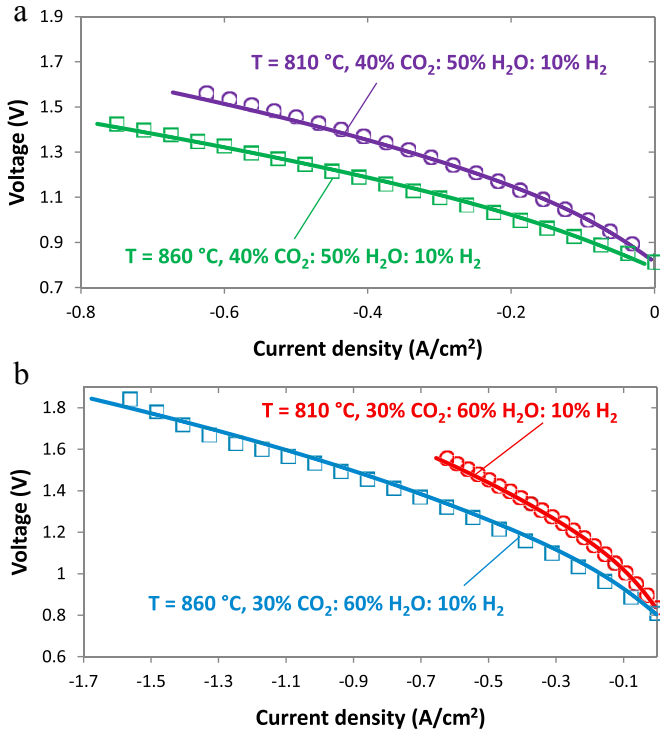


Fig. 4. a: Comparison between numerical simulation and experiments performed at EIFER for an inlet gas composition of 40% CO₂: 50% H₂O: 10% H₂. b: Comparison between numerical simulations and experiments performed at EIFER for an inlet gas composition of 30% CO₂: 60% H₂O: 10% H₂.

Table 4
Electrochemical model/input parameters for experiments done at EIFER.^a

Property	H ₂ –H ₂ O	CO–CO ₂
Fuel electrode asymmetry factor (β_a)	0.7	0.5
Oxygen electrode asymmetry factor (β_a)	0.3	0.45
<i>Exchange current density parameters</i>		
Pre-exponential factor (k_i) (A cm ⁻²)	178763.39	1480354.03
Activation energy (E_i) (J mol ⁻¹)	108.4 × 10 ³	131.38 × 10 ³
Pre-exponential for O ₂ production (k_{O_2}) (A cm ⁻²)	88735.51	
Activation energy for O ₂ production (E_{O_2}) (J mol ⁻¹)	122.5 × 10 ³	

^a Fitted with experimental data.

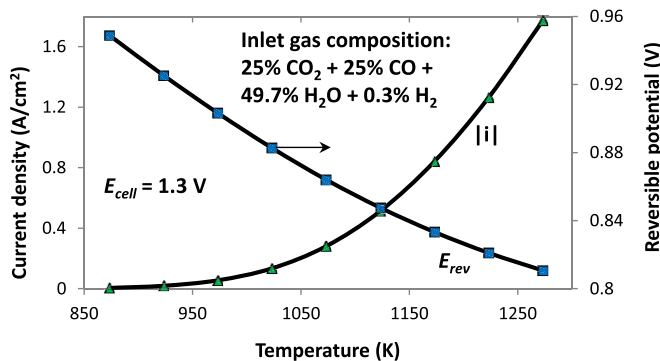


Fig. 5. Effect of temperature on SOEC electrochemical characteristics.

CO–CO₂ mixtures were only slightly higher than co-electrolysis in H₂O–CO–CO₂ mixtures. Also, the ASR values of the cell for co-electrolysis using H₂O–CO–CO₂ mixtures and electrolysis using H₂O–H₂ mixtures were nearly identical. Fig. 4(a) and (b) shows good agreement with experimental data. The model is also able to predict trends in limiting current density, along with experimentally observed ASR values. The electrochemical model parameters used for the reproduction of experimental data are given in Table 4, while details pertaining to cell properties can be found in Table 3. Additionally, the electrochemical parameters deduced from reproduction of experiments carried out at EIFER, from Table 4, are used for further parametric analysis.

4.1.2. Effect of operating temperature on SOEC electrochemical characteristics

The effect of operating temperature on reversible cell potential and normalized net current density is shown in Fig. 5. The net reversible cell potential is given as a function of partial pressures of electrochemical reactants and products at the TPB,

$$E_{rev} = E^0 + \frac{RT}{4F} \ln \left(\frac{p_{H_2,c} p_{CO,c} p_{O_2,a}}{p_{H_2O,c} p_{CO_2,c}} \right) \quad (38)$$

It is interesting to note that the reversible cell potential decreases with increase in temperature, even though an increase in temperature elevates the electrochemical reaction rate leading to increased consumption and production of reactants and syngas, respectively. This rise is offset by the electromotive force at standard pressure E^0 , which decreases with a rise in temperature as the Gibbs free energy ($\Delta G(T)$) available to the system decreases, as the heat energy demand ($T\Delta S$) increases at higher temperatures. The current density increases with an increase in temperature due to a decrease in ohmic and activation overpotentials. It is important to remember that the current densities are actually negative and only the magnitudes are considered for parametric analysis.

4.1.3. Effect of micro-structural properties on SOEC electrochemical characteristics and species distribution in the porous media

The effect of micro-structural parameters on the performance of SOECs and species transport dispersion in the electrode are discussed in this section. Fig. 6(a) depicts the impact of pore size on the system. It can be noted that the current density obtained at a specified voltage increases with an increase in pore diameter. This is due to the direct dependence of the Knudsen diffusion coefficient (Eq. (15)) and permeability (Eq. (14)) on the pore size associated with the porous media. An increase in pore diameter enhances the Knudsen diffusion coefficient, thus making it easier for the reactants to diffuse in to the TPB. The permeability also increases with pore size. This decreases transport limitations within the electrode and enhances the net current density output. Simulations are performed by varying only the required cathode micro-structural properties. The species composition is shown for $E_{cell} = 1.3$ V.

Fig. 6(b) illustrates the impact of porosity on cell characteristics. Inevitably, the current density obtained at a specified voltage increases with an increase in porosity. This is because the concentration overpotential decreases, which facilitates species transport via increase in diffusion and permeability. Thus, there is decreased resistance to reactant transport. It can be seen that there are larger concentrations of electrochemical reactants at the TPB for $\phi = 50\%$, while the concentrations of products at the TPB are larger for $\phi = 20\%$. Thus, there is a trade-off between product build-up at the TPB as opposed to steady supply of fresh reactants through the diffusion pathway, in determining optimum porosity for electrode materials. The surface coverage of electrochemical products is much higher than the surface coverage of reactants due to higher

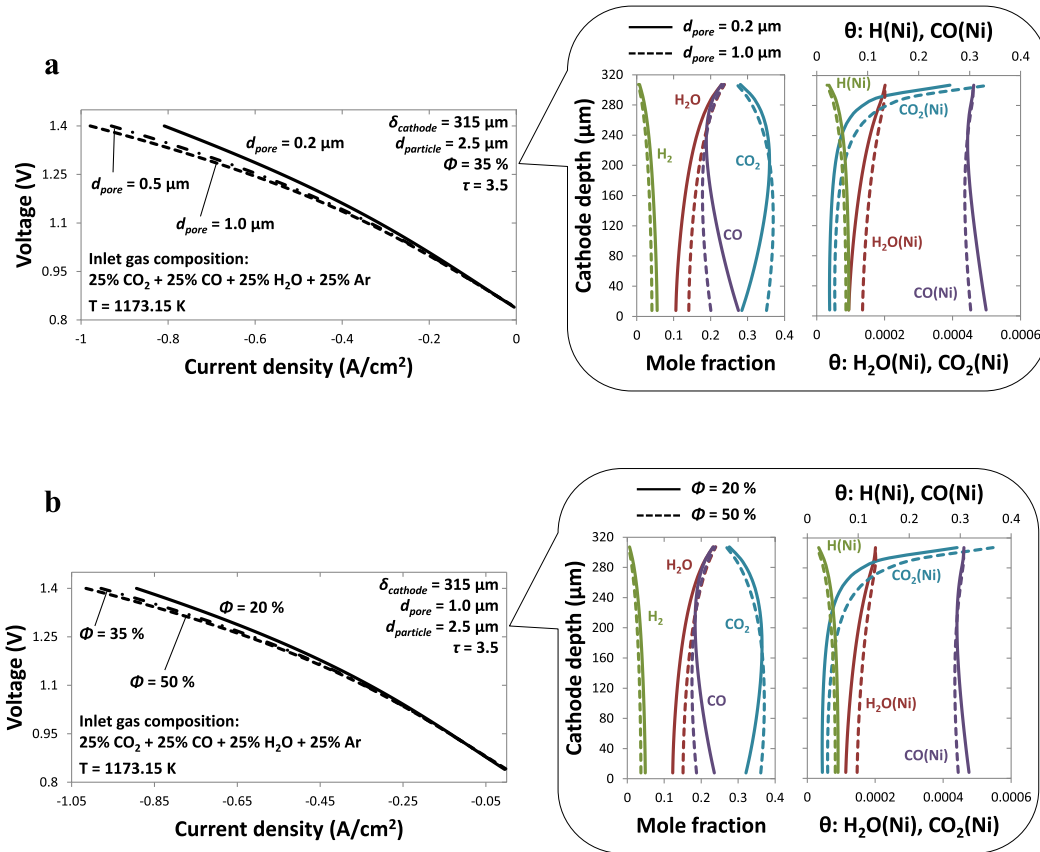


Fig. 6. a: Effect of pore diameter on SOEC $V-I$ characteristics and species distribution in the cathode. b: Effect of porosity on SOEC $V-I$ characteristics and species distribution in the cathode.

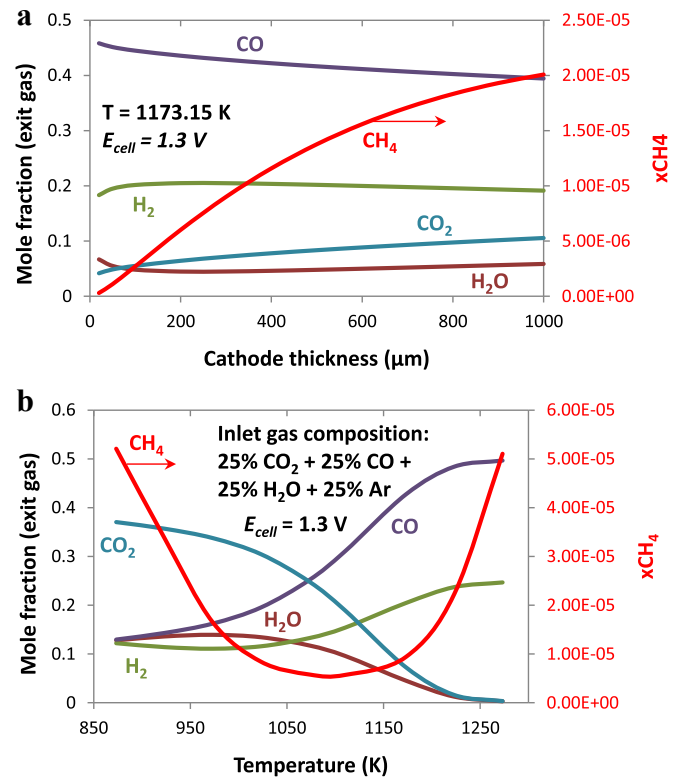


Fig. 7. a: Dependence of cathode exit gas composition on its corresponding electrode thickness. Inlet cathode gas composition: 25% H_2O : 25% CO_2 : 25% CO : 25% Ar . b: Dependence of cathode exit gas composition on temperature.

activation energies required for desorption. Similarly, one can predict the impact of tortuosity on cell $V-I$ characteristics and electrode species distribution. An increase in tortuosity decreases the attainable current density at a specified voltage. This is because the reactants are required to travel through a longer tortuous path to reach the TPB, hence lowering the Knudsen diffusion coefficient and permeability. Thus, one can expect larger electrochemical product concentrations at the TPB for $\tau = 8.0$ as opposed to larger electrochemical reactant concentrations at the TPB for $\tau = 2.0$. Hence, replenishing the TPB with reactants turns harder with increasing tortuosities.

4.2. 1-D + 1-D detailed model

4.2.1. Effect of electrode thickness and temperature on exit gas composition at the cathode

Fig. 7(a) demonstrates the impact of cathode thickness on the outlet gas composition of its corresponding channel. The length of the channel is 5 cm. The inlet gas composition at the cathode channel is 25% H_2O : 25% CO_2 : 25% CO : 25% Ar , where as air is fed to the anode. It can be observed that the mole fraction of H_2 reaches a maximum at $\sim 200 \mu m$, while that of CO is highest at $\sim 20 \mu m$. This is due to the interplay between the electrochemical reactions at the cathode TPB (utilization region), internal reforming (heterogeneous chemistry) zone and transport limitations within the porous electrode. Thinner cathodes result in an overlap between the electrochemical zone and the internal reforming zone, wherein the latter zone is limited by presence of shorter diffusion pathways to the former zone. The initial increase in H_2 mole fraction for thinner cathodes ($< 200 \mu m$) is due to the presence of short diffusion pathways for H_2O to migrate to the electrochemical reaction zone,

while the mole fraction of CO still decreases due to slower diffusion of heavier CO₂ and lower possibility for the RWGS reaction to occur. As the cathode thickness increases (>~200 μm), the mole fractions of H₂ and CO decrease due to transport limitations leading to higher concentration overpotentials, despite the electrochemical zone having negligible influence on the steady state species concentrations in the internal reforming zone. The concentration of CH₄ increases slightly with an increase in cathode thickness due to higher carbon coverage C_(Ni) within the porous electrode, close to the TPB, owing to a highly reducing atmosphere.

Fig. 7(b) describes the influence of temperature on the exit gas composition obtained in the cathode channel. The length of the channel is 5 cm. The general trend encompasses a decrease in the mole fraction of reactants, alongside an increase in that of products, with an increase in temperature. The electrochemical reaction rates are enhanced due to a reduction in irreversible losses, which lead to the attainment of higher current densities. The mole fraction of CO is greater than that of H₂ due to the contribution of both electrolysis and the RWGS reaction. Also, it is important to note that the inlet gas contains more carbon (CO + CO₂) than hydrogen atoms. On closer observation, one can notice an increase in H₂O mole fraction, and a decrease in H₂ mole fraction, for temperatures between ~873.15 and ~1050 K. This is due to the equilibrium between the WGS and RWGS reaction that is attained above ~873.15 K on Ni catalysts. The mole fraction of CH₄ decreases from ~873.15 to 1073.15 K, and then increases from ~1073.15 to 1273.15 K, though it is quite small. At lower temperatures, the Boudouard reaction along with the hydrogenation of elemental carbon C_(Ni) is favored. A highly reducing atmosphere contributes to CH₄ formation at higher temperatures, due to the presence of large concentrations of CO and H₂ [39].

4.2.2. Effect of inlet gas velocity on the performance of a SOEC

Fig. 8(a) explains the impact of inlet gas velocity, in the cathode channel, on SOEC performance parameters. The reactant utilization factor η_{R-U} is given by

$$\eta_{R-U} = 100 \times \left[1 - \frac{(\dot{n}_{H_2O} + \dot{n}_{CO_2})_{outlet}}{(\dot{n}_{H_2O} + \dot{n}_{CO_2})_{inlet}} \right] \quad (39)$$

The oxygen production factor η_{O-P} is defined as

$$\eta_{O-P} = 100 \times \left[\frac{(Y_{O_2})_{outlet}}{(Y_{O_2})_{inlet}} - 1 \right] \quad (40)$$

The reactant utilization factor decreases, while the oxygen production factor increases, with an increase in cathode inlet gas velocity. Thus, the amount of reactant available at the TPB increases, although the electrochemical reaction rate at a given voltage limits the amount of reactant that can be converted. This decreases the reversible cell potential (Eq. (38)), which translates to the attainment of a higher normalized current density. As the electrochemical fluxes are directly proportional to current density (Eq. (36)), higher concentrations of oxygen are obtained at the exit of the anode gas channel. The variation in axial gas concentrations as a function of cathode inlet gas velocity can be seen in Fig. 8(b). High inlet velocities lead to reactant wastage. Hence, a trade-off between syngas production rates and reactant utilization factors is necessary to avoid performance penalties and degradation.

4.2.3. Significance of the type of electrolysis on species composition in the cathode and its corresponding channel

The effect of H₂O electrolysis (CO₂ electrolysis pathway is turned off) coupled with detailed chemistry, and H₂O/CO₂ co-electrolysis coupled with detailed chemistry, on the profiles of gas and surface species within the cathode and its corresponding channel are depicted in Fig. 9. The operating temperature and voltage are 1173.15 K and 1.3 V, respectively. The concentrations of products increase, while that of reactants decrease, as one moves towards the exit of the gas channel. The reactant utilization and syngas production rate are higher during co-electrolysis, which translates to similar trends within the cathode. The gas concentrations and surface coverage of relevant species are also illustrated. The mole fraction of CH₄, although negligible, is higher during co-electrolysis as compared to the case involving only H₂O electrolysis. This can be attributed to higher carbon coverage C_(Ni) within the porous electrode, which increases in magnitude with increase in axial distance. Adsorbates – H_(Ni) and CO_(Ni) form the major species in the cathode, and decide the concentration of the uncovered Ni surface.

4.3. Possible methane production characteristics and reaction pathways

In this section, we study the kinetics of methane production and factors affecting it. There is existent speculation in literature about formation pathways and experimental data pertaining to the methanation process. In this study, we do not develop an additional model or mechanism, but perform reaction flow analysis and simulations using the surface reaction mechanism in Table 1. A 0-D batch reactor model is used for the aforementioned analysis, whose equations and modeling approach are elucidated in Ref. [26]. The reactor is considered to operate at OCV, and does not account for electrochemistry. The input parameters for all simulations are Volume V = 50 mm³, T = 923.15 K, p = 1 bar and A_{cat} = 28.25 × 10⁻⁴ m². Fig. 10 portrays a comparison between the effect of temperature on the equilibrium composition of methane and on the kinetics described by the surface reaction mechanism.

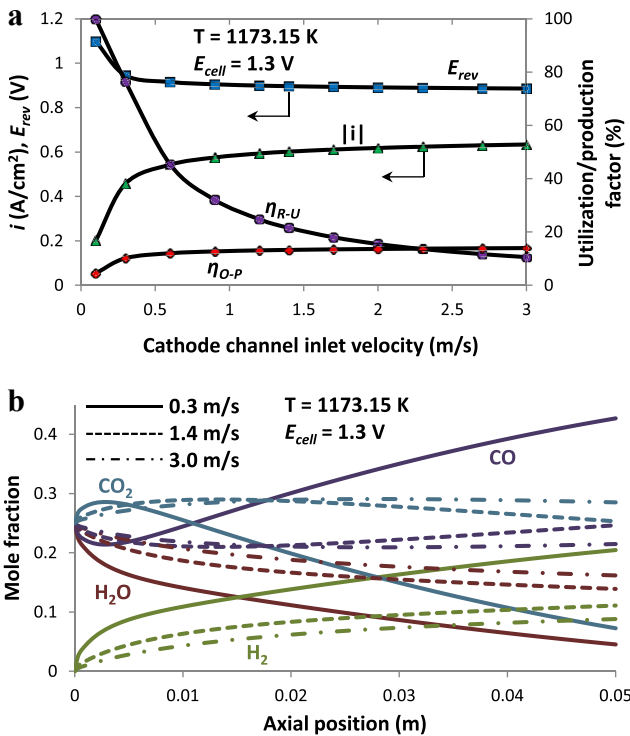


Fig. 8. a: Influence of cathode inlet gas velocity on SOEC process parameters. b: Influence of cathode inlet gas velocity on the axial species composition in the cathode channel. Inlet cathode gas composition for both cases: 25% H₂O: 25% CO₂: 25% CO: 25% Ar.

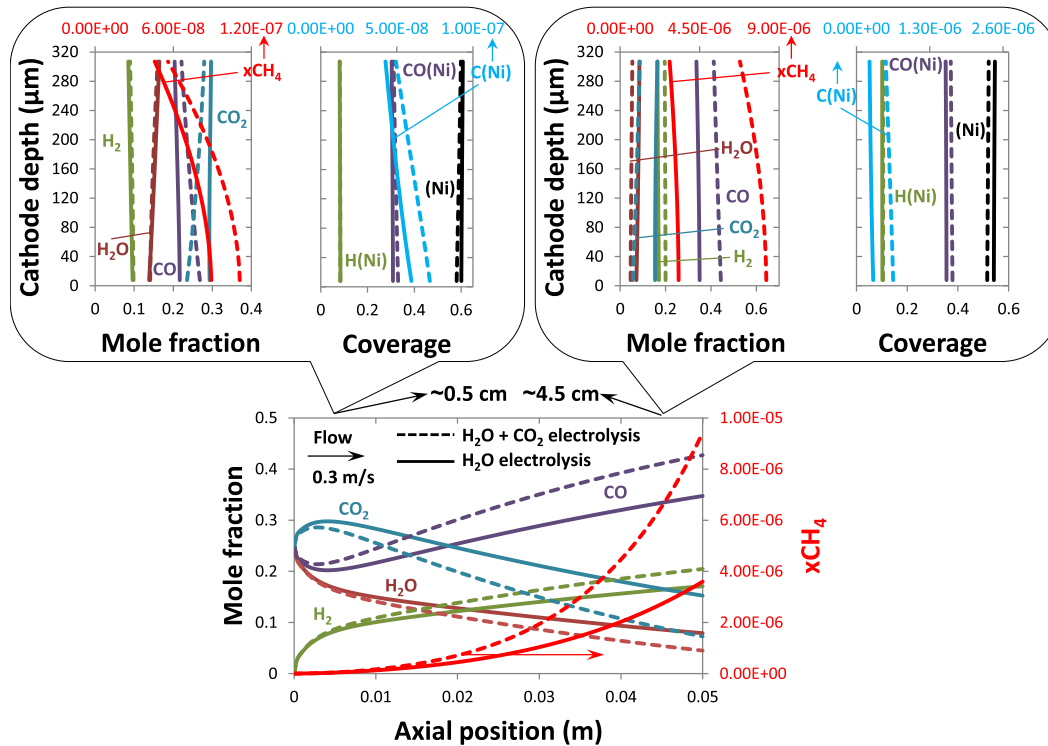


Fig. 9. Importance of the type of electrolysis on species composition in the cathode and its corresponding channel. Inlet cathode gas composition: 25% H₂O: 25% CO₂: 25% CO: 25% Ar.

The equilibrium composition without elemental carbon results in much higher CH₄ mole fraction as compared to the batch model and the simulation considering equilibrium composition with elemental carbon. At low temperatures, the model predictions are close to equilibrium calculations without surface carbon, while at high temperatures, the model predictions are close to equilibrium calculations with surface carbon. The model curves at two different times indicate compositions before and after steady-state. After ~35 s, steady state concentration is reached. It is now established that the model is capable of capturing trends in CH₄ formation, although one requires improvement in the carbon model for accurate predictions. The equilibrium calculations are performed using the commercial software – HSC Chemistry v5.1, while the batch model runs on the module – DETCHEM^{BATCH} [26].

In Fig. 11, one can notice the variation in CH₄ mole fraction as a function of residence time for various fuel compositions listed in Table 5. It can be observed that an increase in the amount of H₂O inhibits the formation of CH₄. Adsorbed H₂O_(Ni) decomposes to H_(Ni)

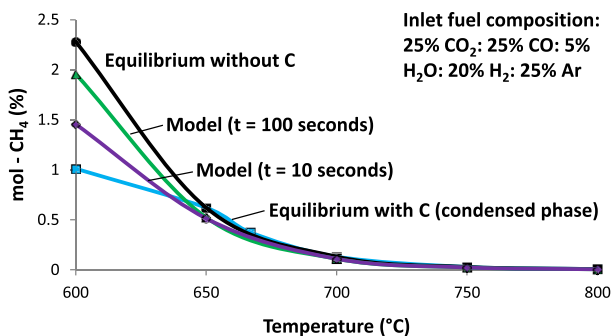


Fig. 10. Effect of temperature on the composition of methane determined by equilibrium calculations and kinetics described by the surface reaction mechanism, for fuel – B in Table 5.

and OH_(Ni) via reaction R32 in Table 1. The adsorbate OH_(Ni) further dissociates to H_(Ni) and O_(Ni). From the results of the reaction flow analysis, it is seen that a greater fraction of adsorbed carbon C_(Ni) is oxidized by O_(Ni) via reaction R35 and is a few orders of magnitude (~10⁴) higher than the contribution of reaction R28 in Table 1. An increase in CO₂ input concentration does not favor CH₄ production, as it demotes the formation of elemental carbon C_(Ni). The highest amount of CH₄ is obtained for fuel-A, which has the largest inlet concentration of H₂ and CO. Consequently, hydrogenation of C_(Ni) is strongly feasible in this case.

Furthermore, reaction flow analysis is carried out, for fuel-A and fuel-B in Table 5, to clearly understand the contribution of participating gas and surface species towards methane formation. In Fig. 12(a), the numbers beside the arrows indicate the amount of species converted. The desorption of adsorbate CO_(Ni) to gaseous CO

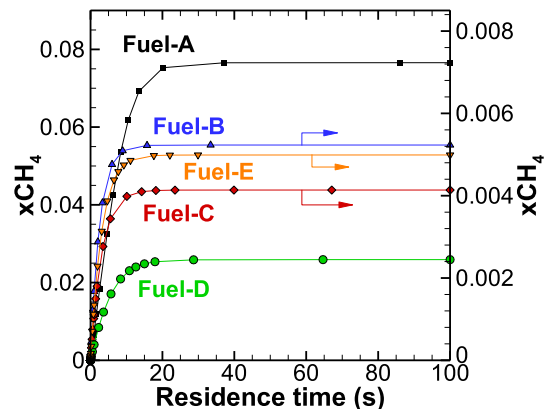


Fig. 11. The variation in CH₄ mole fraction with residence time for various fuel compositions described in Table 5.

Table 5
Fuel compositions considered for batch reactor model simulations.

Fuel	xH ₂ %	xH ₂ O %	xCO %	xCO ₂ %	xAr %
A	40	—	40	5	15
B	20	5	25	25	25
C	20	25	25	25	5
D	40	—	25	25	10
E	40	—	5	40	15

is not considered so as to get the absolute scale of its contribution towards HCO_(Ni), CO_{2(Ni)} and C_(Ni) formation. In this case, the inlet fuel composition is 25% CO₂: 5% H₂O: 20% H₂: 25% CO: 25% Ar (fuel-B) and the residence time is 1.0 s. The majority of the adsorbate CO_(Ni) comes from the dissociation of CO_{2(Ni)} and adsorption of CO. The adsorbed CO_(Ni) then splits into adsorbates – HCO_(Ni), CO_{2(Ni)} and C_(Ni) through surface reactions. The adsorbate HCO_(Ni) has negligible contribution towards CH_(Ni) formation and is the unlikely path towards CH₄ formation. On the other hand, the surface carbon

C_(Ni) undergoes hydrogenation, through reaction R20 in Table 1, to form CH_(Ni). This adsorbate CH_(Ni) reacts with H_(Ni) to form CH_{2(Ni)}, which further reacts in the same manner to form CH_{3(Ni)} and then CH_{4(Ni)} through reactions R18, R16 and R14, respectively. Almost all of the adsorbed CH_{4(Ni)} desorbs to form CH₄ gas. This appears to be the more likely pathway leading to CH₄ formation. In Fig. 12(b), the same analysis is performed for an inlet fuel composition of 5% CO₂: 40% H₂: 40% CO: 15% Ar (fuel-A), while the residence time is 1.0 s. Here, one can notice a higher fraction of adsorbate CO_(Ni) dissociating to surface carbon C_(Ni) and adsorbed oxygen O_(Ni), thereby resulting in a higher mole fraction of CH₄. Simulations performed with other fuel compositions in Table 5 also yield the same trend, even at higher residence times. However, it is important to bear in mind that the thermodynamic properties of elemental carbon/graphite C_(Ni) are different from carbon nanofibers (CNF), which are more likely to occur in the SOC electrode [40]. In addition, the methanation process is also affected by the extent of pretreatment of the Ni catalyst by the oxidation and reduction process [41]. It was

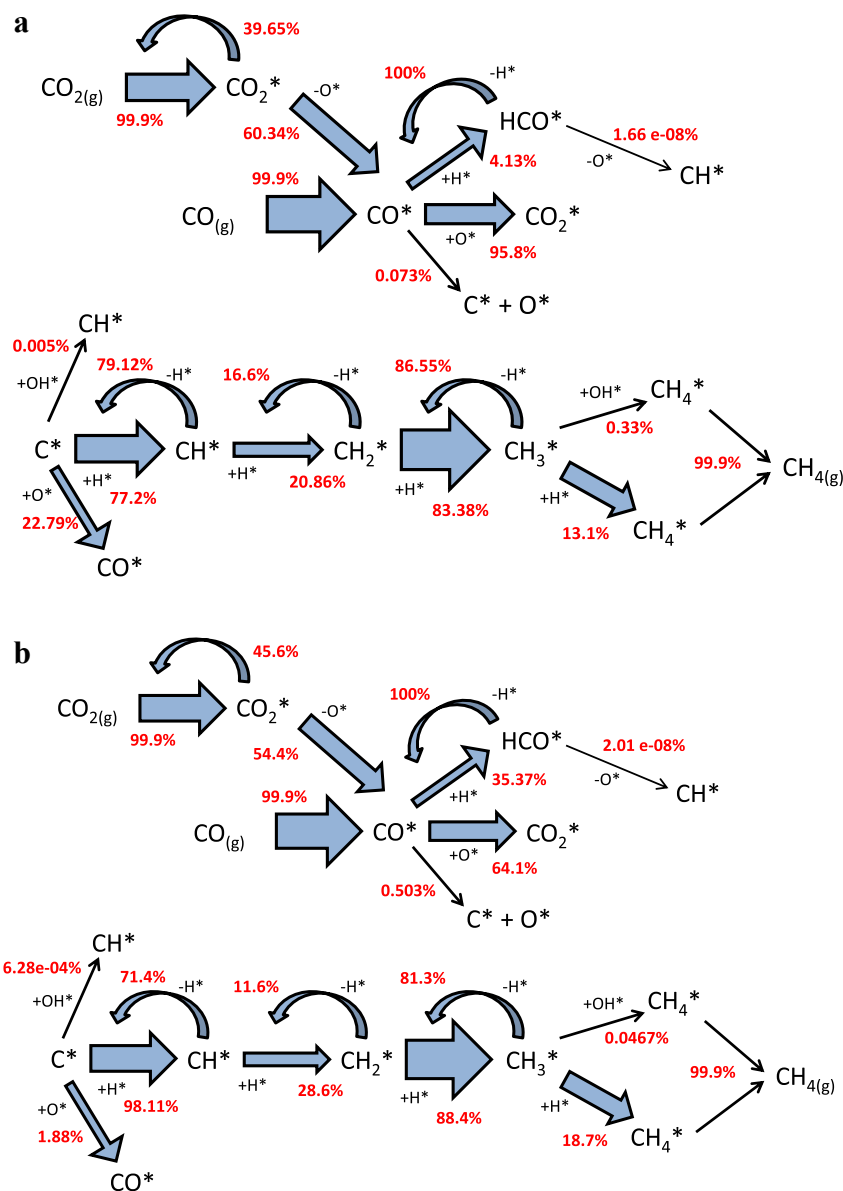


Fig. 12. a: Reaction flow analysis diagram indicating species consumption/production for fuel – B in Table 5. b: Reaction flow analysis diagram indicating species consumption/production for fuel – A in Table 5.

found that the NiO in the pretreated catalyst acted as a promoter and weakened the C–O bond to produce surface carbon that was easily hydrogenated, which led to the formation of more methane. Nevertheless, this study can be considered as a preliminary step towards understanding the complex methane production kinetics in a SOC system.

5. Conclusion

The analysis of high temperature co-electrolysis of H₂O and CO₂, for syngas production, in a SOEC has been carried out using a 1-D electrochemical model and a 1-D + 1-D detailed model. The model is validated with experimental data from two sources. The electrochemical parameters determined from the experiments performed at EIFER are used for additional parametric analysis. A number of output parameters such as syngas production rate, current density, reversible cell potential and efficiency depend strongly on temperature. Micro-structural properties such as tortuosity, porosity and pore diameter tend to affect the SOEC electrochemical characteristics by controlling mass transport within the porous electrode, which in turn affects the concentration overpotentials of the system. High tortuosity, low porosity and low pore diameter result in product buildup at the TPB, denying facilitation for reactant replenishment via the diffusion pathway. Furthermore, the cathode inlet gas flow rate is found to have a significant impact on the operating SOEC current density and channel gas composition due to reactant dilution effects. Therefore, it is important to optimize inlet gas flow rates to minimize depletion, bearing in mind the trade-off with fuel utilization. It was found that the co-electrolysis process produced higher amounts of methane in the gas channel as opposed to the simulation that considered electrolysis of only H₂O with the CO₂ electrolysis pathway turned off at the TPB, for the specified inlet fuel composition, due to the production of higher amounts of reducing H₂ and CO in the system. Also, the former resulted in higher reactant utilization rates. Logical analysis using the surface reaction mechanism was carried out using a batch reactor model to study methane formation characteristics in the system at OCV. Through reaction flow analysis, it was established that reaction R20 in Table 1 (hydrogenation of surface carbon C_(Ni)) was the more likely pathway towards CH₄ formation. Further work would involve investigation into the underlying charge transfer mechanisms of a SOEC during co-electrolysis, and methods to make the model more robust via reaction mechanism improvement, carbon model development, energy balance employment and implementation of an elementary approach for analyzing charge transfer kinetics instead of the conventional B–V approach. Nonetheless, the described model can be viewed as an initial approach towards clearly understanding the dynamics of a SOEC system.

Acknowledgment

We thank the Steinbeis GmbH für Technologietransfer (STZ 240 Reaktive Strömungen) for a cost free academic license of DETCHEM™. We deeply value for all the rewarding exchanges on SOCs with Dr. Alexander Kromp (IWE, KIT). We are also indebted to Dr. L. Maier and Ms. K. Herrera Delgado (ITCP, KIT) for all the fruitful discussions on reaction kinetics. Financial support by the Helmholtz Research School *Energy-Related Catalysis* is gratefully acknowledged.

References

- [1] C. Graves, S.D. Ebbesen, M. Mogensen, K.S. Lackner, *Renew. Sustain. Energy Rev.* 15 (2011) 1–23.

- [2] Q. Fu, C. Mabilat, M. Zahid, A. Brisse, L. Gautier, *Energy Environ. Sci.* 3 (2010) 1382–1397.
- [3] J. Wei, E. Iglesia, *J. Catal.* 224 (2004) 370–383.
- [4] K.R. Sridhar, B.T. Vaniman, *Solid State Ionics* 93 (1997) 321–328.
- [5] A.O. Isenberg, *Solid State Ionics* 3–4 (1981) 431–437.
- [6] W. Doenitz, R. Schmidberger, E. Steinheil, R. Streicher, *Int. J. Hydrogen Energy* 5 (1980) 55–63.
- [7] R.D. Green, C.C. Liu, S.B. Adler, *Solid State Ionics* 179 (2008) 647–660.
- [8] S.H. Jensen, P.H. Larsen, M. Mogensen, *Int. J. Hydrogen Energy* 32 (2007) 3253–3257.
- [9] J. Sigurvinsson, C. Mansilla, P. Lovera, F. Werkoff, *Int. J. Hydrog. Energ.* 32 (2007) 1174–1182.
- [10] V. Menon, V.M. Janardhanan, O. Deutschmann, *Chem. Eng. Sci.* 110 (2014) 83–93.
- [11] G. Tao, K.R. Sridhar, C.L. Chan, *Solid State Ionics* 175 (2004) 615–619.
- [12] G. Tao, K.R. Sridhar, C.L. Chan, *Solid State Ionics* 175 (2004) 621–624.
- [13] S.D. Ebbesen, M. Mogensen, *J. Power Sources* 193 (2009) 349–358.
- [14] M. Ni, *Chem. Eng. J.* 164 (2010) 246–254.
- [15] G. Narasimhaiah, V.M. Janardhanan, *J. Solid State Electrochem.* 17 (2013) 2361–2370.
- [16] C. Stoots, J. O'Brien, J. Hartvigsen, *Int. J. Hydrogen Energy* 34 (2009) 4208–4215.
- [17] S.D. Ebbesen, R. Knibbe, M. Mogensen, *J. Electrochem. Soc.* 159 (2012) F482–F489.
- [18] P. Kim-Lohsoontorn, J. Bae, *J. Power Sources* 196 (2011) 7161–7168.
- [19] Z.L. Zhan, W. Kobsiriphat, J.R. Wilson, M. Pillai, I. Kim, S.A. Barnett, *Energy Fuels* 23 (2009) 3089–3096.
- [20] M. Ni, *J. Power Sources* 202 (2012) 209–216.
- [21] M. Ni, *Int. J. Hydrogen Energy* 37 (2012) 6389–6399.
- [22] W. Li, Y. Shi, Y. Luo, N. Cai, *J. Power Sources* 243 (2013) 118–130.
- [23] W. Li, H. Wang, Y. Shi, N. Cai, *Int. J. Hydrogen Energy* 38 (2013) 11104–11109.
- [24] Y. Xie, X. Xue, *Solid State Ionics* 224 (2012) 64–73.
- [25] Q. Fu, J. Dailly, A. Brisse, M. Zahid, *ECS Trans.* 35 (2011) 2949–2956.
- [26] O. Deutschmann, S. Tischer, S. Kleditzsch, V.M. Janardhanan, C. Correa, D. Chatterjee, N. Mladenov, H.D. Minh, V. Menon, H. Karadeniz, *DETCHEM™ Software Package*, 2.4 ed., 2012. Karlsruhe, <http://www.detchem.com/>.
- [27] V. Menon, V.M. Janardhanan, S. Tischer, O. Deutschmann, *J. Power Sources* 214 (2012) 227–238.
- [28] E.A. Mason, A.P. Malinauskas, *Gas Transport in Porous Media: the Dusty Gas Model*, Elsevier, New York, 1983.
- [29] R. Suwanwarangkul, E. Croiset, M.W. Fowler, P.L. Douglas, E. Entchev, M.A. Douglas, *J. Power Sources* 122 (2003) 9–18.
- [30] J. Bear, *Dynamics of Fluids in Porous Media*, American Elsevier, New York, 1972.
- [31] H. Zhu, R.J. Kee, *J. Power Sources* 169 (2007) 315–326.
- [32] H. Zhu, R.J. Kee, V.M. Janardhanan, O. Deutschmann, D.G. Goodwin, *J. Electrochem. Soc.* 152 (2005) A2427–A2440.
- [33] J. Aicart, J. Laurencin, M. Petitjean, L. Dessemond, in: *Proceedings of the Fundamentals and Developments of Fuel Cells Conference (FDCC)*, April 16–18 2013. Karlsruhe, Germany.
- [34] V. Menon, V.M. Janardhanan, O. Deutschmann, *ECS Trans.* 57 (2013) 3207–3216.
- [35] L. Maier, B. Schädel, K. Herrera Delgado, S. Tischer, O. Deutschmann, *Top. Catal.* 54 (2011) 845–858.
- [36] V.M. Janardhanan, O. Deutschmann, *J. Power Sources* 162 (2006) 1192–1202.
- [37] V.M. Janardhanan, O. Deutschmann, *Chem. Eng. Sci.* 62 (2007) 5473–5486.
- [38] P. Deufhard, E. Hairer, J. Ziegler, *Numer. Math.* 51 (1987) 501–516.
- [39] Y. Tao, S.D. Ebbesen, M.B. Mogensen, *J. Electrochem. Soc.* 161 (2014) F337–F343.
- [40] W.Y. Lee, J. Hanna, A.F. Ghoniem, *J. Electrochem. Soc.* 160 (2013) F94–F105.
- [41] S.H. Kim, S.W. Nam, T.H. Lim, H.I. Lee, *Appl. Catal. B Environ.* 81 (2008) 97–104.

Nomenclature

- A_c : area of cross section of flow channels (m²)
 A_s : specific area (m⁻¹)
 B_g : permeability (m²)
 C_p : specific heat (J kg⁻¹ K⁻¹)
 d_p : particle diameter (m)
 d_{pore} : pore diameter (m)
 D : diffusivity (m² s⁻¹)
 D_{eff}^{bin} : effective binary diffusion (m² s⁻¹)
 D_h : hydraulic diameter (m)
 D_{eff}^{Kn} : effective Knudsen diffusion (m² s⁻¹)
 E_{cell} : cell voltage (V)
 E_{rev} : reversible cell potential (V)
 F : Faraday constant (C mol⁻¹)
 h : heat transfer coefficient (J m⁻² K⁻¹ s⁻¹); specific enthalpy (J kg⁻¹)
 H_c : channel height (m)
 ΔH : enthalpy of formation (J mol⁻¹)
 H : mixture enthalpy (J mol⁻¹)
 i : current density (A cm⁻²)

J_k : species flux ($\text{mol m}^{-2} \text{s}^{-1}$)
 K_g : number of gas-phase species
 n : number of charge transferred
 \dot{n}_i : molar flow rate (mol s^{-1})
 p : pressure (Pa)
 P_e : MEA perimeter (m)
 R : gas constant ($\text{J mol}^{-1} \text{K}^{-1}$)
 R_{ct} : charge transfer resistance (Ωcm^2)
 \dot{s} : molar production rate ($\text{mol m}^{-2} \text{s}^{-1}$, $\text{mol m}^{-3} \text{s}^{-1}$)
 ΔS : entropy change (J K^{-1})
 t : time (s)
 T : temperature (K)
 v : velocity (m s^{-1})
 V_{OC} : open-circuit voltage (V)
 V_m : thermo-neutral voltage (V)
 W_{k_i} : molecular weight of k th species (kg mol^{-1})
 $[X]$: concentration (mol m^{-3})
 x, y, z : co-ordinate direction (m)
 X : mole fraction
 Y : mass fraction

Greek letters

γ : normalization factor for current density
 δ : Kronecker delta symbol

η : overpotential
 θ : surface coverage fraction
 μ : viscosity ($\text{kg m}^{-1} \text{s}^{-1}$)
 ρ : density (kg m^{-3})
 τ : tortuosity
 ϕ : porosity

Subscripts

c : channel
 e : electrolyte/electrode
 f : fluid
 k : species index

Abbreviation

DGM : dusty-gas model
 MEA : membrane electrode assembly
 TPB : three-phase boundary
 $B-V$: Butler–Volmer
 ASR : area-specific resistance
 LHV : lower-heating value
 SOC : solid-oxide cell